Contents lists available at ScienceDirect

Journal of Manufacturing Processes

journal homepage: www.elsevier.com/locate/manpro

# Microstructure and mechanical properties of wire-powder hybrid additive manufacturing for high nitrogen steel

Tongli Wu [a,c], Jie Liu [b,c,*], Kehong Wang [b,c], Liangmo Wang [a], Xiaoyong Zhang [a,*]

[a] School of Mechanical Engineering, Nanjing University of Science and Technology, Nanjing 210094, China
[b] School of Materials Science and Engineering, Nanjing University of Science and Technology, Nanjing 210094, China
[c] Key Laboratory of Controlled Arc Intelligent Additive Manufacturing Technology, Nanjing University of Science and Technology, Nanjing 210094, China

ARTICLE INFO

*Keywords:*
Wire-powder arc additive manufacturing
High nitrogen steel
Microstructure and mechanical properties

ABSTRACT

A novel wire-powder hybrid arc additive manufacturing (WPHAAM) was applied for melting zone nitridizing to avoid the deterioration effect caused by the loss of nitrogen in high nitrogen steel. A designed Cr-Mn-N wire with 0.79 wt% of nitrogen (HNS6) was used to build a high nitrogen wall body by introducing WPHAAM method. The influence of nitrogen content on solidification behavior, microstructure, and tensile properties were studied in the as-built conditions. With the increase of amount of feeding powder, the solidification mode of the deposited wall changes from primary ferrite with second-phase austenite (FA mode) to primary austenite with second-phase ferrite (AF mode), and the mechanical properties are enhanced. When the powder feeding rate reaches 0.33 g/min, the solidification changes to A mode, and the deposited metal is austenite. The ultimate tensile strength and elongation of the deposited metal are 1014 MPa and 50.8% respectively.

## 1. Introduction

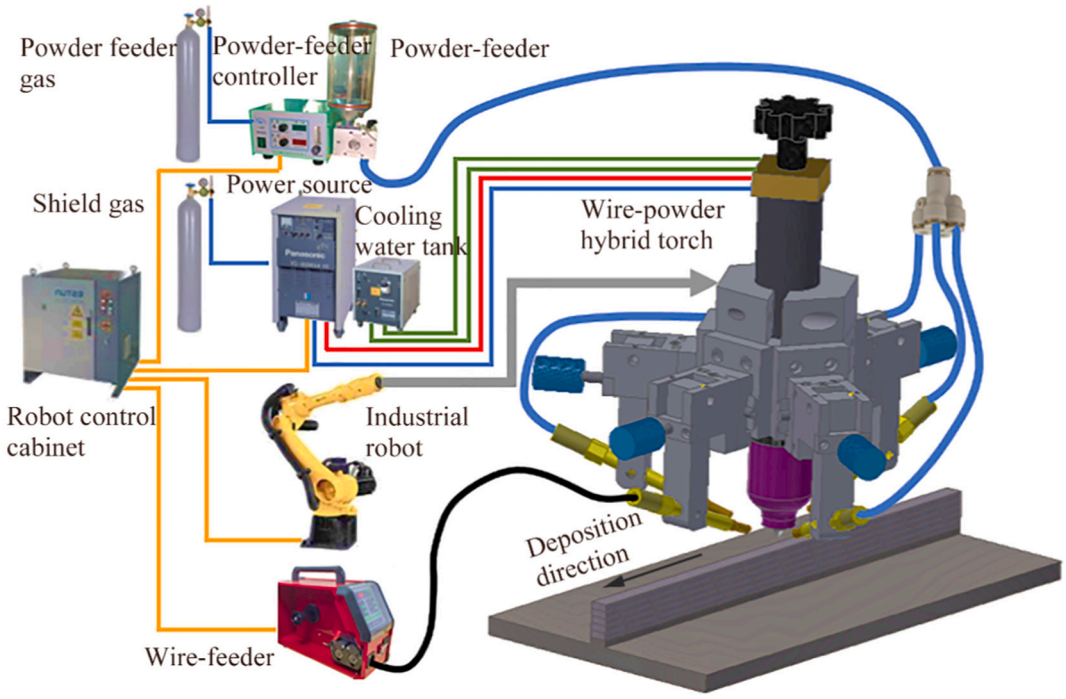
High nitrogen austenitic stainless steel (HNSS) is a new type of steel that applies nitrogen instead of nickel as main austenitizing element [1]. Compared with conventional stainless steel, HNSS has the advantage of superior tensile strength, outstanding corrosion resistance, high work-hardening performance, and good biocompatibility [2]. It can be applied in construction building, marine engineering and biological materials [3]. The supersaturated nitrogen tends to precipitate in the welding process, which results in serious nitrogen loss and reduction of mechanical performance of high nitrogen steel. Over the past several decades, there are many researchers focusing on raising solid-saluted nitrogen content in the weld bead, to avoid its loss in the form of nitride or pores. There are some methods applied such as (1) chemical composition improvement for higher nitrogen solubility [4–7]; (2) shielding gas optimization by either increasing the nitrogen partial pressure [8–12] or adding surface-active elements like oxygen [13] or multi-component gas mixture [14–16] in the welding process; (3) using nitride flux-cored wire as a feeding material during welding [17,18].

Although these methods can reduce the nitrogen loss in the welding process of high nitrogen steel to a certain extent, the nitrogen content of the welded joint or the deposited metal is lower than that of the base metal or the filling material. It is still a challenge to improve the nitrogen content of deposited metal or welded joint to exceed that of filler or base metal. This work introduces a novel concept of a wire-powder TIG arc additive manufacturing (WPHAAM) process to obtain a pure austenite structure with ultra-high nitrogen content. In this method, HNSS welding wire and nitride alloy powder are simultaneously fed into a tungsten-argon arc welding pool by means of side-shaft conveying. When the nitride powder dissolves in the molten pool, it dissociates and adsorbs, an additively manufactured steel with ultra-high nitrogen content is obtained.

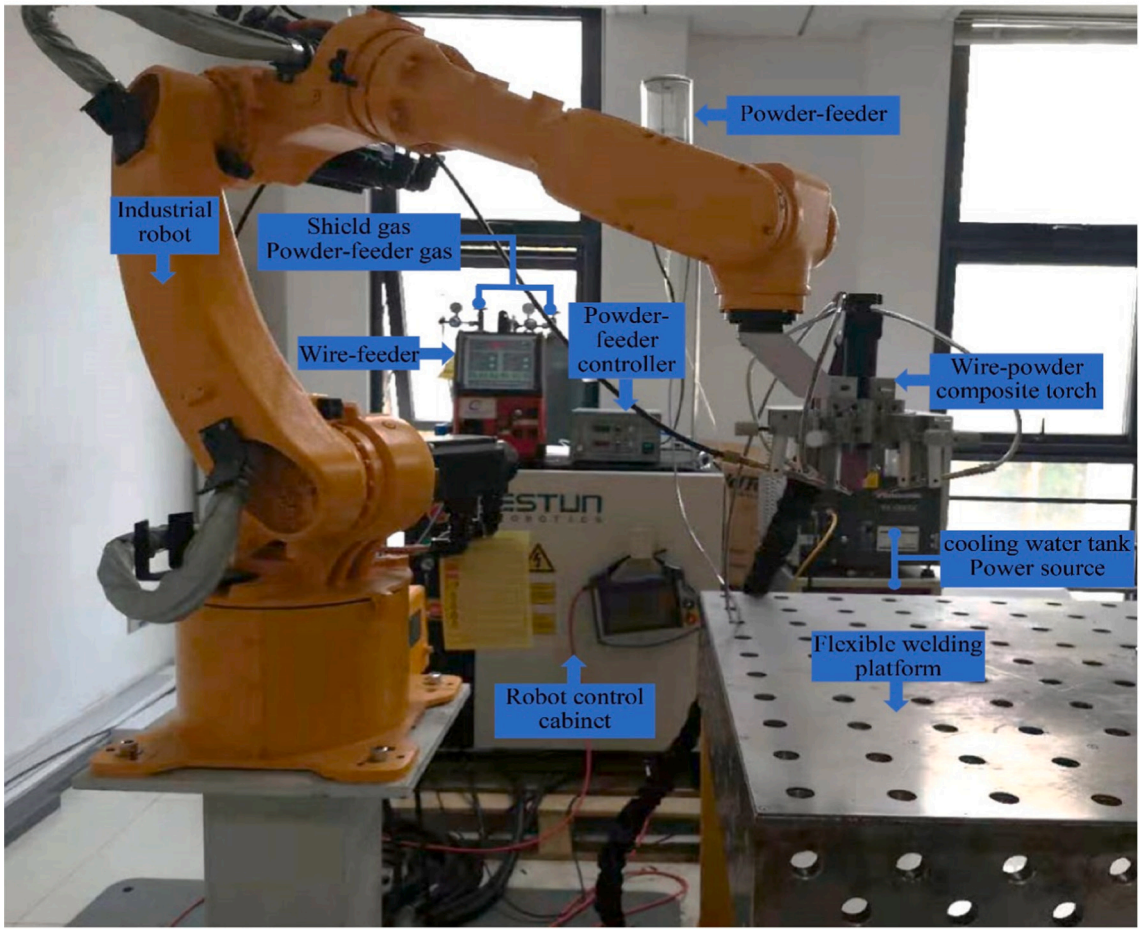
In this work, the microstructure and mechanical properties of the deposited metal with wire-powder hybrid TIG arc additive manufacturing process at different powder feeding rates are comprehensively evaluated and studied by comparative analysis. Four groups of deposited walls are prepared by the WPHAAM processes. By analyzing the bead appearance, metallography, grain size, fractography, and mechanical properties, the unique characteristics of the WPHAAM process are determined. This research provides a new way for nitrogen fixation and nitrogen increase of high nitrogen austenitic stainless steel welding or additive manufacturing, and the results of experiments and discussions can also be used as a reference for developing special welding materials for high nitrogen austenitic stainless steel.

* Corresponding authors at: School of Materials Science and Engineering, Nanjing University of Science and Technology, Nanjing 210094, China
*E-mail addresses:* j.liu@njust.edu.cn (J. Liu), xiaoyong.zhang@njust.edu.cn (X. Zhang).

https://doi.org/10.1016/j.jmapro.2021.08.029
Received 16 June 2021; Received in revised form 3 August 2021; Accepted 21 August 2021
1526-6125/© 2021 The Society of Manufacturing Engineers. Published by Elsevier Ltd. All rights reserved.




(a) Schematic diagram of experimental apparatus




(b) Experimental setup

**Fig. 1.** The robot wire-powder GTAW arc additive manufacturing process system.

**Table 1**
Chemical composition of homemade HNS6 wire used in this test.

| Material | Chemical composition (wt%) | | | | | | | | |
|---|---|---|---|---|---|---|---|---|---|
| | C | N | S | P | Mn | Cr | Ni | Mo | Fe |
| HNS6 | 0.066 | 0.79 | 0.008 | 0.018 | 16.79 | 21.66 | 2.18 | 1.25 | Residual |

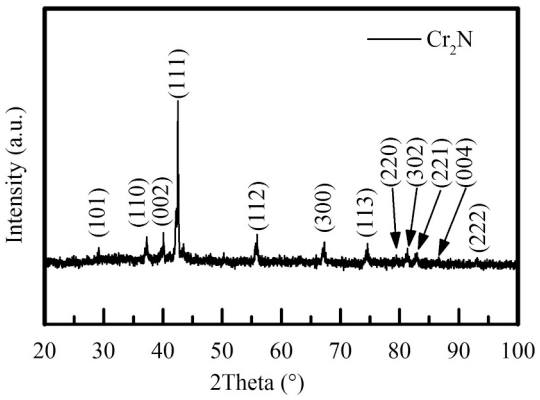



**Fig. 2.** X-ray diffraction patterns of the $Cr_2N$ powder.

**Table 2**
WPHAAM process parameters.

| Notation | Parameter | |
|---|---|---|
| Arc length | 8 mm | |
| Current | 150 A | |
| Wire feeding rate | 100 cm/min | |
| Arc running rate | 7.5 cm/min | |
| Shielding gas | 20 L/min | |
| Powder feeding rate | No powder (sample 1) | 0.22 g/min (sample 2) |
| | 0.33 g/min (sample 3) | 0.41 g/min (sample 4) |
| Tungsten diameter | 5 mm | |
| Interface temperature | below 100 °C | |

## 2. Experiment procedure

### 2.1. Experimental setup

A robotic wire-powder arc additive manufacturing system, as described in Fig. 1(a), is used to fabricate the components. It consists of a 400 A GTAW power source (Panasonic YC-300WX4), a water-cooled GTAW welding torch mounted on a 6-axis industrial robot (ESTUN ER12-1510), a powder-feeder device, and automatic constant-wire feeder equipment to ensure consistent GTAW arc deposition. The experiment setup is shown in Fig. 1(b). Three powder-feeding nozzles with an angle of 120° are coaxal with the GTAW welding torch. A wire feeder is placed between two powder feeding nozzles, in the welding direction is used for wire feeding.

### 2.2. Material preparation and WPHAAM process

The used HNS6 steel wire is casted, rolled, and drawn into wire with a diameter of 1.2 mm. An annealing process is followed with a temperature of 1000 °C for 1 h. The chemical composition of the HNS6 wire is listed in Table 1. A plain carbon steel plate with a dimension of 150 × 80 × 6 mm is used as the base metal.

Pure $Cr_2N$ (99.9%) is used as feeding powder in the wire-powder arc additive deposition process. The X-ray diffraction pattern of the $Cr_2N$ powder is shown in Fig. 2. The D50 diameter of the original particle size of the $Cr_2N$ powder is about 60 μm.

In order to study the effects of the nitrogen content on microstructure, and mechanical properties of the high nitrogen austenite stainless steels, four experimental groups with different feeding rates are implemented. These process parameters are listed in Table 2.

Arc running speed (ARS) is fixed as 7.5 cm/min with the wire feed speed (WFS) of 1 m/min. Pure argon (99.99%) is used as a shielding gas and powder feeding gas at a constant flow rate of 20 L/min and 0.8 L/min, respectively. The surface of the substrate is ground to remove the oxide layer. The organic matter on its surface is cleaned with acetone. Deposited layers are built by moving the GTAW welding torch and feeding wire into the molten pool. A reparative deposition method, that the starting location of the next deposit layer is the same as the previous layer, is used in this experiment. During the deposition process, an offset of 8 mm is found to be suitable for wire-powder feeding to the melt pool. The additive-manufactured multi-layer samples are approximately 110 mm long. Each sample is composed of 7 layers with a height of about 10 mm.

### 2.3. Metallographic and mechanical property test

Samples for metallographic observation, nitrogen content measurement, and tensile tests are cut from the deposited wall by electro-discharge machining. The location and size of the specimens are shown in Fig. 3. The nitrogen content is measured by an inorganic elemental analyzer inductar ONH cube, with a standard measuring deviation of 0.15 ppm. Four samples for nitrogen content measurement, each 100–120 mg in weight, are taken from each deposited wall. The average value is taken as the nitrogen content of the deposited wall. Metallographic samples are ground, polished, and eroded by ferric chloride hydrochloric acid aqueous solution with 15 g $FeCl_3$, 50 mL HCl and 100 mL $H_2O$ for austenite metallographic observations. Metallurgical specimens are observed by optical microscope (Olympus BX51M). Two plates of 2 mm in thickness with a gap of 2 mm vertically between each are cut horizontally for X-ray diffraction (XRD, Bruker-AXS D8 Advance) analysis with Cu Kα radiation (λ = 1.5418 Å) to observe the phases within each layer. The root layer is cut 2 mm above the base material. Tensile tests are conducted on WE-300 computer-controlled electrohydraulic servo universal testing machine at room temperature.

## 3. Results and discussion

### 3.1. Surface morphology and macrostructure of welds

The appearance of WPHAAM deposition of HNASS with different powder feeding rates is shown in Fig. 4. It can be seen that the surfaces of all the deposition metals exhibit a typical metallic color. The weld surface is well-formed, flat, and smooth without feeding $Cr_2N$ powder, while the deposited metal surface is rough and wrinkled after feeding $Cr_2N$ powder. Because the airflow transporting the $Cr_2N$ powder disturbs the stable combustion of the arc and results in unstable deposition, which causes rough and wrinkled surface. No pores are observed on the top surface of samples 1–3. As the powder feeding rate increases up to 0.41 g/min, a few small pores are found to distribute on the center of the welding seam.

### 3.2. Nitrogen content of the deposited metal

The nitrogen content of feeding wire and samples 1–4 are measured

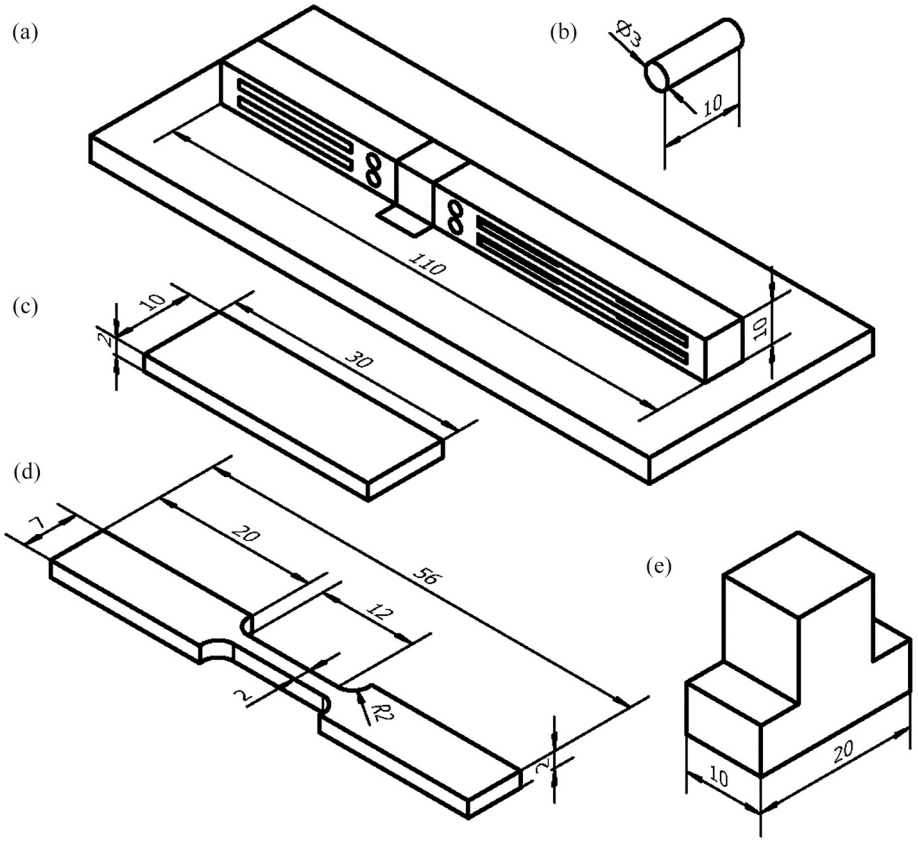



**Fig. 3.** Schematic of the position and the size of the specimens. (a) Schematic diagram of sampling location. (b) Dimensions of nitrogen content test samples. (c) Dimensions of XRD samples. (d) Dimensions of tensile specimens. (e) Dimensions of Metallographic sample.

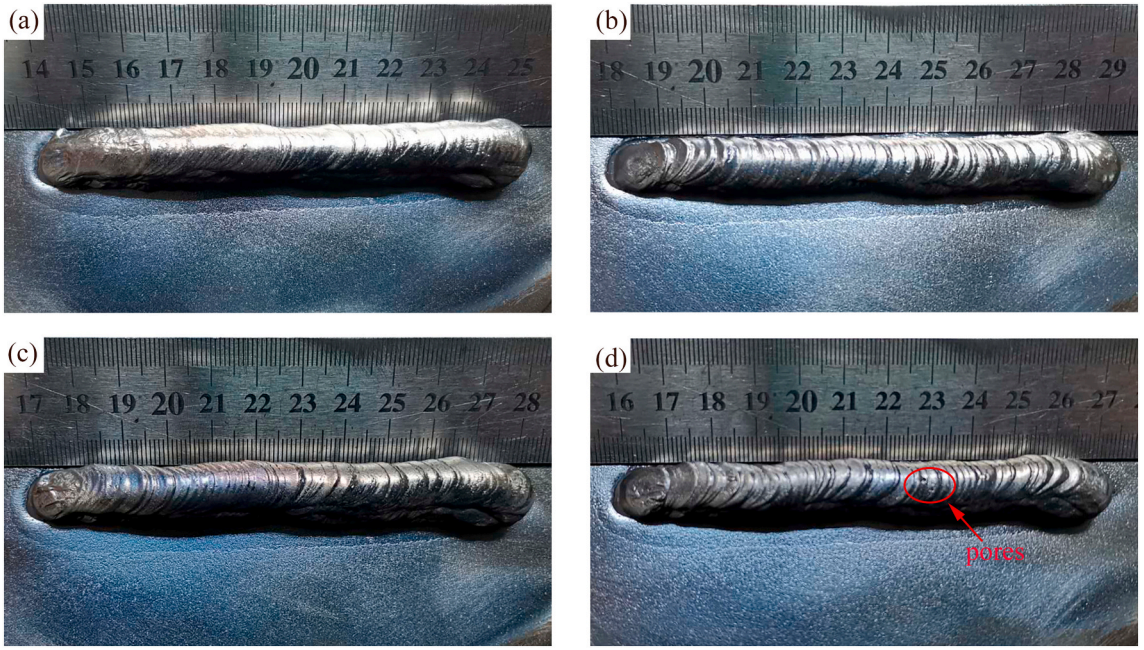



**Fig. 4.** Macroscopic view of additive manufactured samples with different powder feeding rates: (a) sample 1, without powder feeding, (b) sample 2 powder feeding rate 0.22 g/min, (c) sample 3 powder feeding rate 0.33 g/min, (d) sample 4 powder feeding rate 0.41 g/min.

as shown in Fig. 5. When the only wire is used as raw material, the nitrogen content is 0.65% in the deposited wall. Compared with its original nitrogen content (0.79%), there is a loss of 17.7% of solid dissolved nitrogen from the molten zone. With the help of feeding $Cr_2N$ powder into the weld pool, the nitrogen content has been improved obviously from 0.65% to 0.99% at 0.22 g/min, with an increase of 52.3%. However, the increase of nitrogen content does not rise further with acceleration, only to 1.04% at 0.33 g/min and to 1.07% at 0.41 g/min,

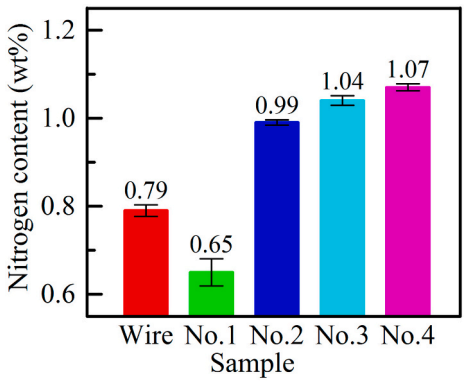



**Fig. 5.** Nitrogen content of feeding wire and samples 1–4.

increased by 5% and 3% compared with the previous step.

### 3.3. Macrostructure

It is known that stainless steel alloys solidify in one of four different modes: single-phase austenite (A), primary austenite with second-phase ferrite (AF), primary ferrite with second-phase austenite (FA), and single-phase ferrite (F) [19]. These solidification modes can be determined by optical metallographic examination of the microstructure as revealed by standard polishing and etching techniques. The deposited metal solidifies completely to austenite (γ) and no further solid transformation takes place during cool process in mode A. For the AF mode, the austenite is the leading phase and δ ferrite, if any, solidifies from the rest melt between the austenite grain boundary. So in AF mode, the ferrite is located at the intersection of austenite dendrites. The

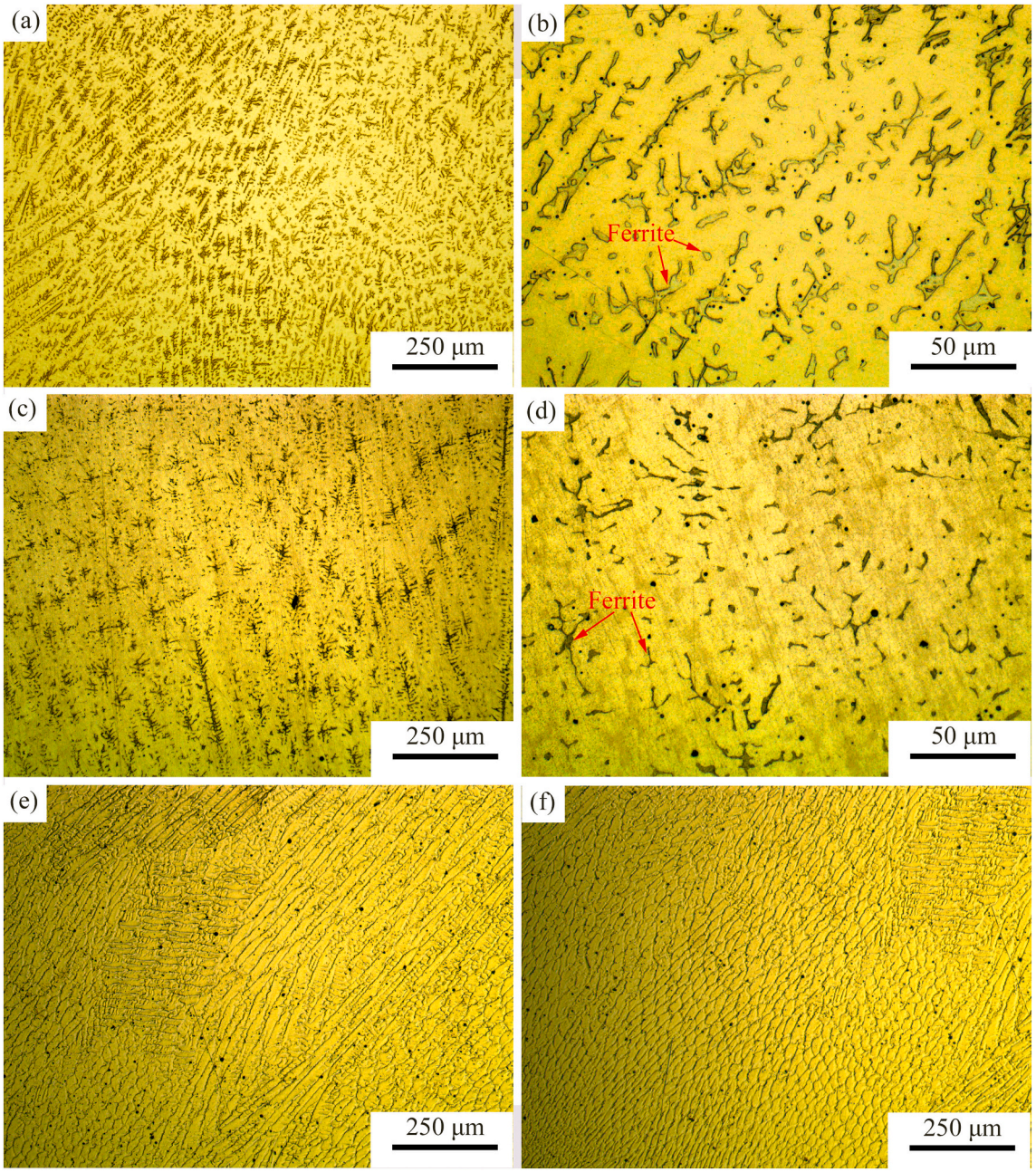



**Fig. 6.** Microstructure of sample 1–4: (a, b) sample 1, without powder feeding, (c, d) sample 2 powder feeding rate 0.22 g/min, (e) sample 3 powder feeding rate 0.33 g/min, (f) sample 4 powder feeding rate 0.41 g/min.

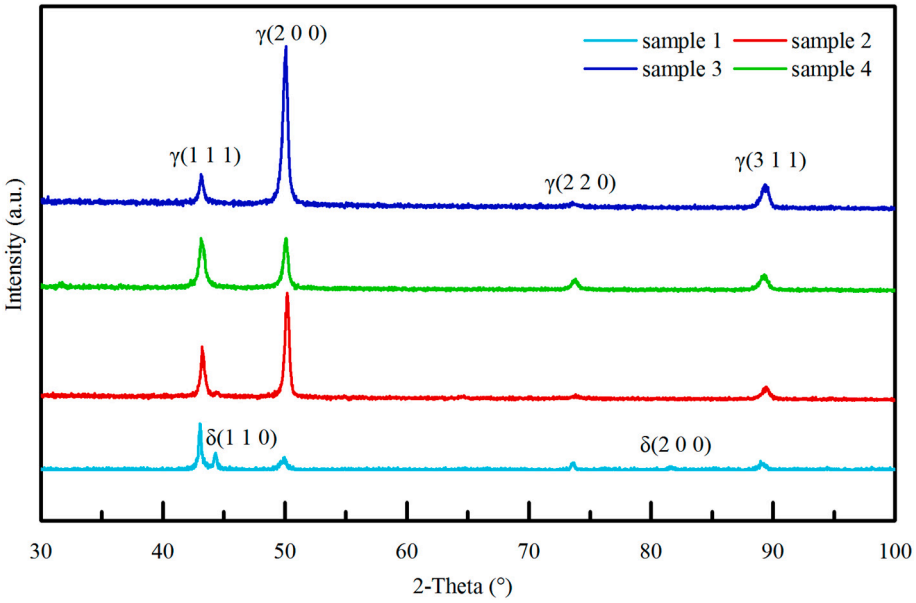



**Fig. 7.** The XRD results of samples 1–4.

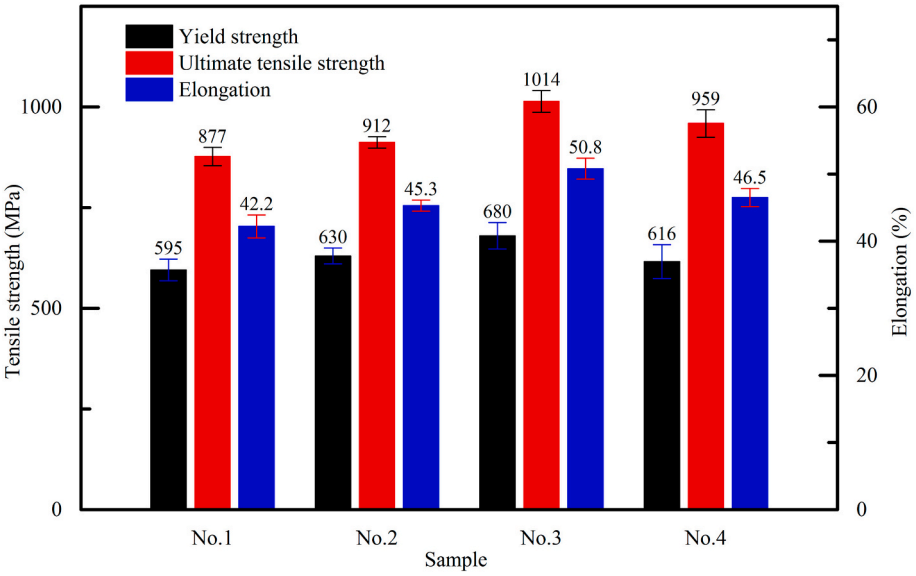



**Fig. 8.** Tensile strength and elongation of the samples.

solidification phase transformation of the deposited metal in FA mode is probably the inverse of this. The ferrite is the leading phase and austenite solidifies from the rest melt. At lower temperature the majority of the ferrite is transformed to austenite either in an equiaxial or acicular morphology, depending on the supercooling of ferrite. In FA mode, ferrite is located in the center of dendrite [20,21].

The metallographic diagram of samples 1–4 is shown in Fig. 6. It is obvious that with the increase of the $Cr_2N$ powder, the ferrite content decreases significantly. When the feeding rate of the $Cr_2N$ powder reaches 0.33 g/min, the ferrite disappears and becomes full austenite.

Fig. 6(a)–(d) shows dendritic microstructure. In Fig. 6(b), the arrow indicates the ferrite skeleton is surrounded by austenite. The skeleton was broken up during the ferrite to austenite transformation, leaving a few isolated round islands, which was the ferrite dendritic arm cut through perpendicular direction. The microstructure of ferrite presents a random vermiform appearance. The ferrite skeleton in Fig. 6(b) shows an average width of 8.4 μm. In Fig. 6(d), the arrow shows the remaining ferrite forms at the austenite grain boundary. The ferrite is partially thin (<0.5 μm) and partially thick (>10 μm), which is a typical morphology of solidified austenite grain boundaries. The growth of ferrite is restricted by austenite grains, and it is not able to form a uniform width. It is thus inferred from microstructure that the solidification mode is FA in Fig. 6(b) and AF in Fig. 6(d).

Fig. 6(e) and (f) is composed of cellular austenite grains. The overall appearance of the microstructure is a regular array of cells appearing as a hexagonal mesh. The difference in microstructure of (e) and (f) derives from the growth direction of grains. If samples are sectioned from a perpendicular direction, the grains can be rectangular or trapezoidal in shape [21]. As no ferrite is observed, it can be determined that the solidification mode in Fig. 6(e) and (f) is typically A mode.

### 3.4. XRD phase analysis

The XRD results with different powder feeding quantities are shown

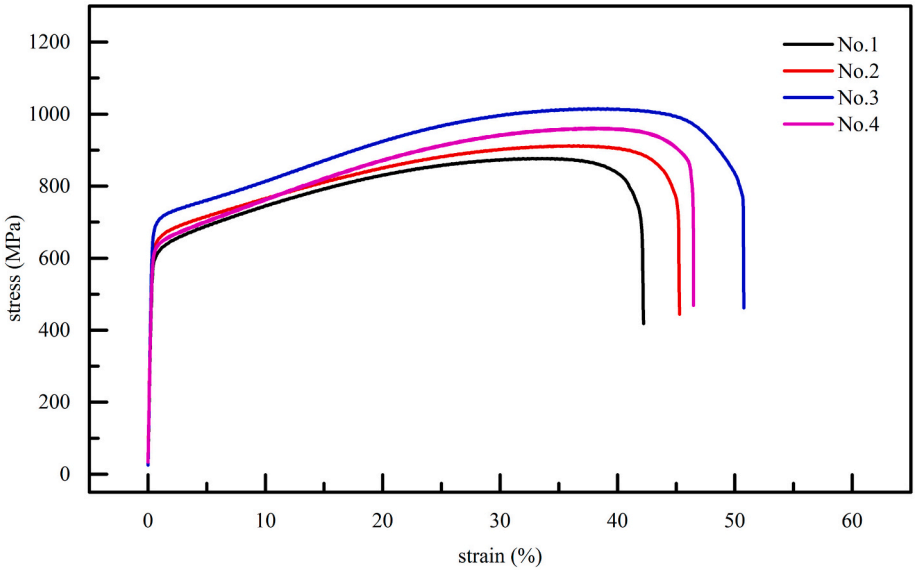



**Fig. 9.** The true stress-stain curves of the samples.

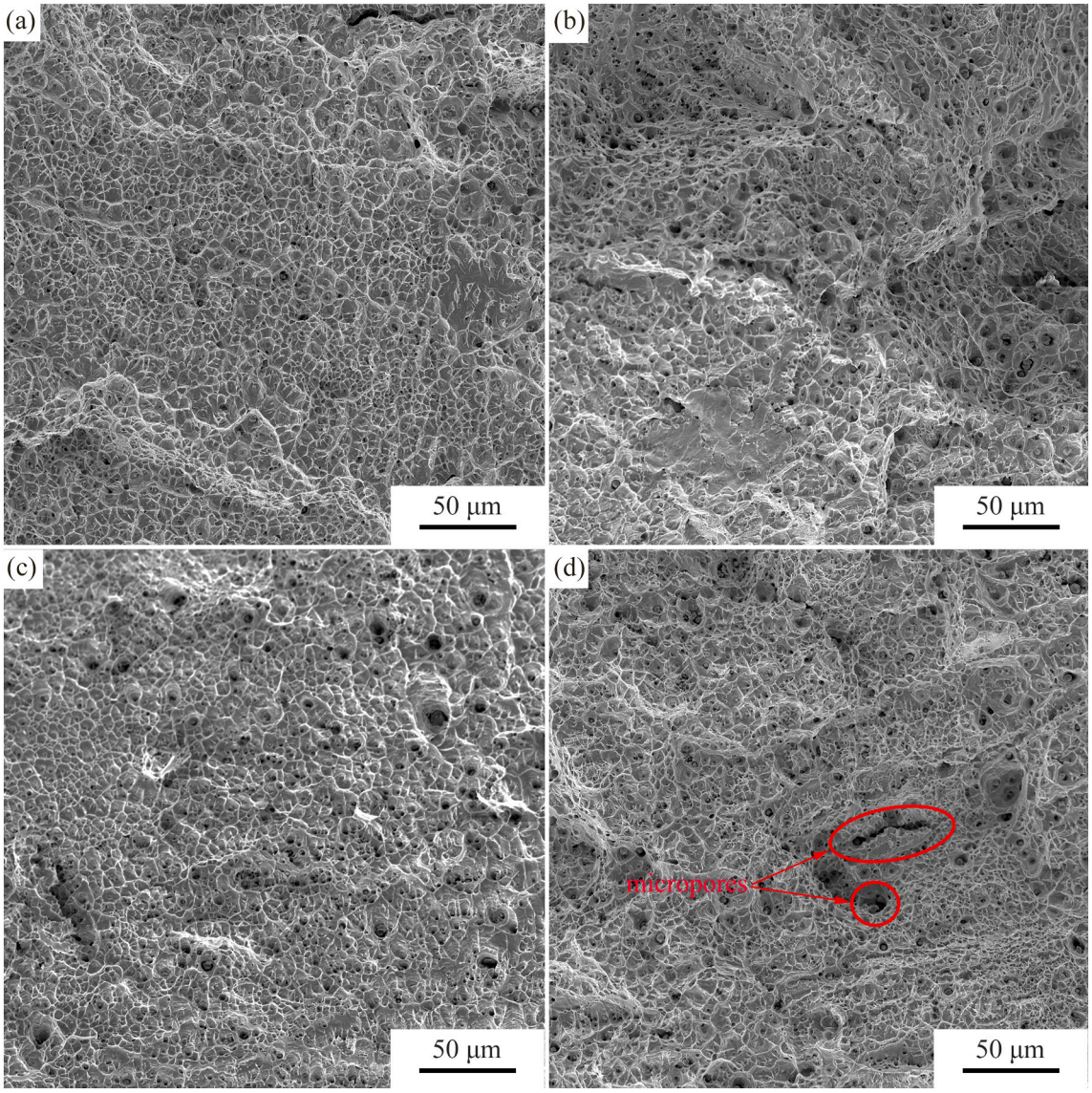



**Fig. 10.** Tensile microscopic fracture morphology: (a) sample 1, (b) sample 2, (c) sample 3 and (d) sample 4.

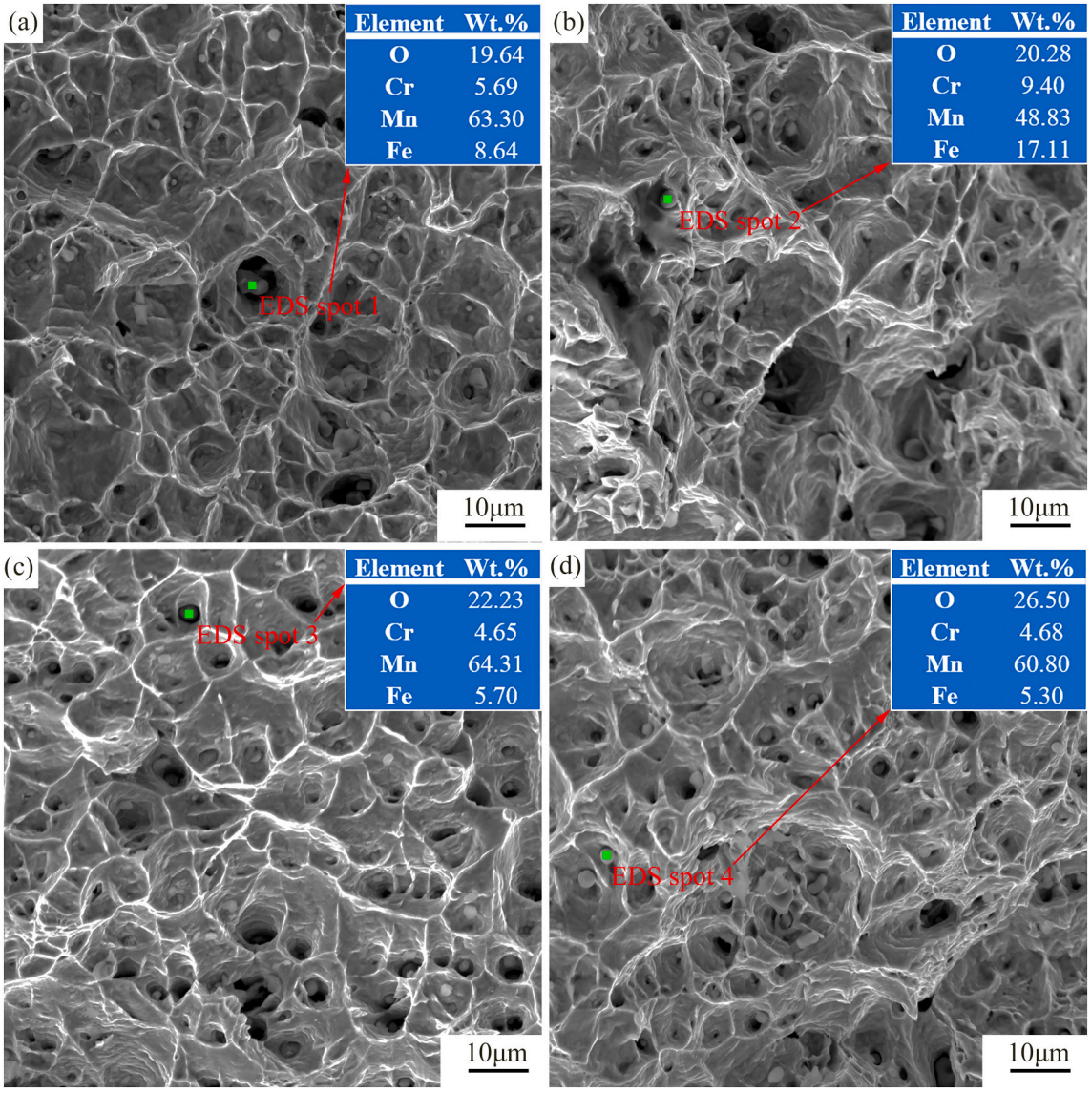



**Fig. 11.** The fractography of samples: (a) sample 1, (b) sample 2 (c) sample 3, and (d) sample 4.

in Fig. 7. Both samples 1 and 2 are composed of austenite + ferrite, while samples 3 and 4 are austenite. Since the area of ferrite diffraction peak is proportional to its content, the ferrite content decreases with the increase of the $Cr_2N$ feeding rate. When the $Cr_2N$ powder feeding speed reaches 0.33 g/min, the ferrite content in the deposited metal reduces to 0, which is consistent with the metallographic observation.

### 3.5. Mechanical properties

#### 3.5.1. Tensile properties

The tensile strength and elongation of the samples 1–4 are shown in Fig. 8. When no $Cr_2N$ is added into the melt, the tensile strength of the deposited metal is 877 MPa. After adding $Cr_2N$ into the weld pool, the tensile strength has been improved obviously. When the $Cr_2N$ feeding rate reaches 0.33 g/min, the ultimate tensile strength was improved from 877 MPa to 1014 MPa, increased by 15.6%. This is related to the ferrite reduction and the uniformity of the deposited metal. The true stress-strain curve is shown in Fig. 9.

#### 3.5.2. Fracture morphology

The tensile fracture morphology of samples 1–4 is exhibits in Figs. 10 and 11. The observations of the microscopic fracture morphology of the samples demonstrate that all the fracture modes are microporous aggregation fractures under uniaxial tensile testing at room temperature. There are many isotropic dimples and a large number of fracture surfaces with deeply torn edges. The morphology of the fractures contained typical characteristics of dimples which indicated that the fractures are ductile failures. There are particles within dimples, and the EDS analysis illustrates that the particle is Chromium ferromanganese oxide inclusion, as shown in Fig. 11. In this case, the number of dimples per unit area on the fracture surface depends on the number of nucleation sites and the plasticity of the material.

Compared with sample 1, the morphology of dimples in samples 2–4 are significantly larger and deeper. They distribute uniformly on the fracture surface, indicating that the samples with feeding $Cr_2N$ powder show better ductility. It is caused by the reduction of ferrite content in the deposited metal. As the feeding rate of $Cr_2N$ powder increases, the dimples become bigger and deeper. On the other hand, there are a few micropores in Fig. 10(d), which promotes the generation of high-density initial pores. In Fig. 10(d), wide dimples should be an indication of large initial voids created by the fracture of micropores.

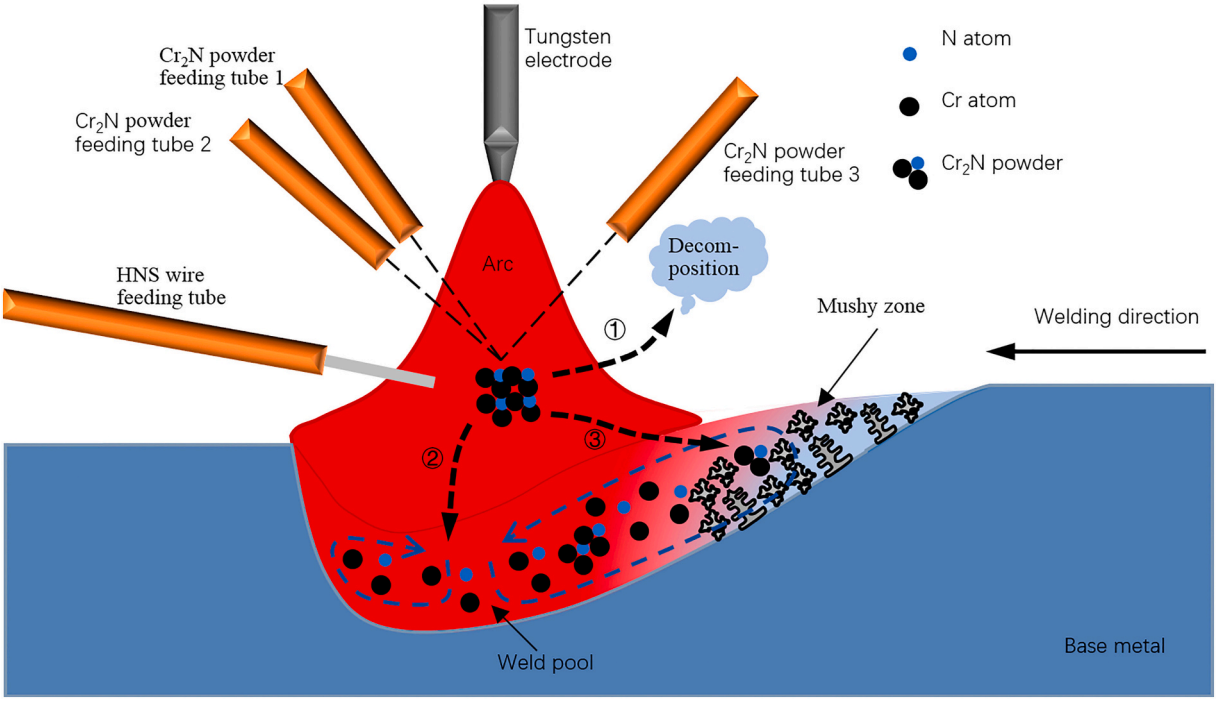



**Fig. 12.** The dissolution process of chromium nitride powder.

### 3.6. Discussion

It can be seen from the metallographic structure shown in Fig. 6, with the increase of powder feeding rate, the content of ferrite in the deposited metal decreases significantly or disappears. Meanwhile, the microstructure changes from dendritic to cellular. The grain size is obviously refined.

The dissolution process of chromium nitride powder is shown in Fig. 12. The whereabouts of $Cr_2N$ powders can be mainly divided into three parts. When the nitride powder enters the arc region, a few $Cr_2N$ particles decompress into free nitrogen and Cr in the arc due to the high temperature of the arc. This increases the nitrogen partial pressure in the protective atmosphere, which is beneficial to increase nitrogen in the molten pool [22–24].

After entering the molten pool, most of the nitride powder particles decompose under the high temperature of the molten pool and become free nitrogen and chromium, which are evenly distributed under the stirring action of the molten pool. This greatly increases the nitrogen content of the molten pool and is beneficial to the nitrogen fixation in the molten pool. With the increase of powder feeding rate, the content of solid solution nitrogen in the deposited metal also increases, which is beneficial to the improvement of mechanical properties on the one hand [25,26] and changes the solidification mode of the deposited metal on the other hand. The model of WRC1992 proposed by Kotecki etc. in 1992 has been widely used to determine solidification mode according to the ratio of Cr-Ni equivalent. The calculation formula of Cr equivalent and Ni equivalent are shown in Eqs. (1) and (2) [27–29].

$$Cr_{eq} = 1Cr + 1.5Mo + 1.5W + 0.48Si + 2.3V + 1.75Nb + 2.5Al \quad (1)$$

$$Ni_{eq} = 1Ni + 30C + 18N + Co + 0.1Mn - 0.0086Mn^2 \quad (2)$$

The principle is to determine the solidification mode according to the Cr-Ni equivalent ratio. When $Cr_{eq}/Ni_{eq} < 1.25$, the solidification mode is A mode; when $1.25 < Cr_{eq}/Ni_{eq} < 1.48$, the solidification mode is AF mode; when $1.48 < Cr_{eq}/Ni_{eq} < 1.95$, the solidification mode is FA mode; when $1.95 < Cr_{eq}/Ni_{eq}$, the solidification mode is F mode. According to the above formula and composition of the deposited metal of samples 1–4, the $Cr_{eq}/Ni_{eq}$ is calculated as 1.55, 1.35, 1.20, and 1.24, respectively. Therefore, due to the loss of nitrogen, the solidification mode of sample 1 is FA mode. By feeding different amounts of $Cr_2N$ powder, the composition and solidification mode of the deposited metal are changed, so that sample 2 is AF mode, and samples 3 and 4 are A mode, which is consistent with the metallographic diagram. The solidification mode changes from FA mode to AF mode or even A mode.

There are some $Cr_2N$ particles larger than 100 μm in size. They may partially decompose in the molten pool, however, they are not completely melted. They could serve as heterogeneous nucleation sites in the mushy zone, which helps to refine the grain size [30].

The nucleation rate N, i.e. the frequency of nucleus formation per unit volume and unit time and heterogeneous nucleation work on the pre-existing surface of the particles may be respectively expressed as [31].

$$N \sim exp\left(-\frac{\Delta G^*}{RT}\right) \quad (3)$$

$$\Delta G^*_{het} = \frac{1}{4}(2+\cos\theta)(1-\cos\theta)^2 \Delta G^*_{hom} \quad (4)$$

where $\Delta G^*$ is the critical nucleation work, $\Delta G_{hom}{}^*$ is the homogeneous nucleation work, $\theta$ is the contact angle, with $0 \ll \theta \ll \pi$ and thus $\Delta G_{het}{}^* \leq \Delta G_{hom}{}^*$. Because of the strong exponential dependence of N on the work of nucleation, the heterogeneous nucleation rate is much larger than the homogeneous nucleation rate, which promotes nucleation and leads to refine the grain size. The grain size of samples 1–4 is refined from 50.1 μm to 25.7 μm with the increase of the powder feeding amount. According to the Hall-Petch formula, the ultimate tensile strength increases with a reduction of grain size, which is consistent with the tensile mechanical properties.

The nitrogen atom is 0.15 nm in diameter and occupies octahedral interstitial sites in the crystal lattice of austenite [32]. It causes lattice distortion and hinders the dislocation movement on the slip plane, which can effectively improve the material strength. It has been suggested that the solid solution strengthening in metals $\sigma_{ss}$ depends on the concentration of solute atoms dissolved in the matrix C as [33,34].

$$\sigma_{ss} = HC^n \quad (5)$$

where C is the concentration of solute atoms homogeneously distributed in the matrix, H and n are constants. The nitrogen content of samples 1–4 increased from 0.65% to 1.07% with the increase of powder feeding amount. According to Eq. (5), the ultimate tensile strength of the alloy increases with the increase of nitrogen content, which is consistent with the tensile mechanical properties of the alloy.

In summary, the strengthening and toughening mechanisms of the wire-powder arc additive manufacturing process are mainly solid-solution strengthening and grain refinement strengthening. On the one hand, most of the chromium nitride particles are completely dissolved after entering the molten pool, which can supplement the nitrogen content of the molten pool metal and increase the solution nitrogen content of the deposited metal. On the other hand, a small amount of incomplete dissolved chromium nitride particles flows to the mushy zone to become heterogeneous nuclei under the action of molten pool agitation, which can reduce the nucleation energy, increase the nucleation rate of molten pool metal, and refine the deposited metal grains. The mechanical properties of deposited metals are greatly enhanced under the dual action of solid-solution strengthening and fine grain strengthening.

## 4. Conclusions

In this study, the wire-powder hybrid TIG arc additive method was used to fabricate a straight wall. The effect of chromium nitride on microstructure and mechanical properties of deposited metal is investigated. At the end of the article, the strength and toughness mechanism of the wire-powder TIG arc additive method is discussed. The following conclusions are drawn:

1. When raw HNS6 wire is used for TIG arc additive, the nitrogen loss rate of the deposited metal is as high as 17.7%, the solidification mode is FA mode, the tensile strength is 877 MPa, and the elongation is 42.2%.
2. The nitrogen content of the deposited metal with high nitrogen wire-powder hybrid arc additive is increased obviously. With the increase of the powder feeding rate, the solidification mode of the deposited metal changes from FA to AF to A, and the ferrite content decreases significantly. When the feeding speed reaches 0.33 g/min, the ferrite disappears, and the deposited metal becomes full austenite.
3. Compared with raw HNS6 wire TIG arc additive, the mechanical properties of the deposited metal with high nitrogen wire-powder hybrid arc additive are obviously improved. When the feeding rate of $Cr_2N$ powder is 0.33 g/min, the ultimate tensile strength and elongation of the deposited metal are 1014 MPa and 50.8% respectively.
4. The analysis shows that the toughening mechanism of high nitrogen wire-powder hybrid arc additive is a comprehensive result of solid solution strengthening and fine grain strengthening.

## Data availability

The raw/processed data required to reproduce these findings cannot be shared at this time as the data also forms part of an ongoing study.

## CRediT authorship contribution statement

Dr. Tongli Wu: Investigation, Conceptualization; Data curation; Formal analysis, Roles Writing original draft, Funding acquisition. Associate professor Jie Liu: Writing review & editing. Professor Kehong Wang: Project administration, Supervision. Professor Liangmo Wang: Supervision. Dr. Xiaoyong Zhang: Data curation, Funding acquisition.

## Declaration of competing interest

The authors declare no conflicts of interest.

## Acknowledgment

This work is supported by the Fundamental Research Funds for the Central Universities, No. 309201B8812, and China Postdoctoral Science Foundation, No. 2021M691588.

## References

[1] Stein G, Hucklenbroich I. Manufacturing and applications of high nitrogen steels. Mater Manuf Process 2004;19(1):7–17.
[2] Simmons JW. Overview: high-nitrogen alloying of stainless steels. Mater Sci Eng A 1996;207(2):159–69.
[3] Ren Y, Yang K, Zhang B, Wang Y, Liang Y. Nickel-free stainless steel for medical applications. J Mater Sci Technol 2004;20(5):571–3.
[4] Mohammed R, Reddy GM, Rao KS. Effect of filler wire composition on microstructure and pitting corrosion of nickel free high nitrogen stainless steel GTA welds. Trans Indian Inst Met 2016;69(10):1919–27.
[5] Gawlik J, Schmidt J, Nowak T, Wójcicki Z, Zagórski A. Nitrogen as an alloying element improving material properties of the high carbon cast steel for ball mill liner plates. Arch Civ Mech Eng 2017;17(4):926–34.
[6] Wendler M, Weiß A, Krüger L, Mola J. Effect of manganese on microstructure and mechanical properties of cast high alloyed Cr M n N i-N steels. Adv Eng Mater 2013;15(7):558–65.
[7] Liu Z, Fan C, Chen C, Yang C, Lin S, Wang L. Design and evaluation of nitrogen-rich welding wires for high nitrogen stainless steel. J Mater Process Technol 2021;288:116885.
[8] Kikuchi Y, Matsuda F, Okabe T, Ohta M. Nitrogen content of 316L weld metal and its fine particle by means of high-pressure MIG Arc welding. ISIJ Int 1996;36:977–82.
[9] Kuwana T, Kokawa H, Matsuzaki S. Nitrogen absorption into weld metal under welding atmosphere of high pressure (part 2) - nitrogen absorption into stainless steel weld metal under welding atmosphere of high pressure. Quart J Jpn Weld Soc 1985;3:744–51.
[10] Zhao L, Tian Z, Peng Y. Porosity and nitrogen content of weld metal in laser welding of high nitrogen austenitic stainless steel. ISIJ Int 2007;47:1772–5.
[11] Qiang W, Wang K. Shielding gas effects on double-sided synchronous autogenous GTA weldability of high nitrogen austenitic stainless steel. J Mater Process Technol 2017;250:169–81.
[12] Liu Z, Fan C, Ming Z, Chen C, Liu A, Yang C, et al. Gas metal arc welding of high nitrogen stainless steel with Ar-N2-O2 ternary shielding gas. Defence Technol 2021;17(3):923–31.
[13] Du Toit M, Pistorius P. The influence of oxygen on the nitrogen content of autogenous stainless steel arc welds. Weld J (Miami, Fla) 2007;86:222s–30s.
[14] Elmer J, Vaja J, Carlton H, Pong R. The effect of Ar and N2 shielding gas on laser weld porosity in steel, stainless steels, and nickel. Weld J 2015;94:313s–25s.
[15] Cui B, Zhang H, Jia Liu, Zhang F. Study on the impact of the shielding gas on the droplet transfer mode and blowhole defect of high nitrogen steel welding. J Mech Eng 2017;53(22):87–94.
[16] Yang D, Huang Y, Fan J, Jin M, Peng Y, Wang K. Effect of N2 content in shielding gas on formation quality and microstructure of high nitrogen austenitic stainless steel fabricated by wire and arc additive manufacturing. J Manuf Process 2021;61:261–9.
[17] Liu Z, Fan C, Chen C, Ming Z, Liu A, Yang C, et al. Optimization of the microstructure and mechanical properties of the high nitrogen stainless steel weld by adding nitrides to the molten pool. J Manuf Process 2020;49:355–64.
[18] Du Toit M, Pistorius P. Nitrogen control during the autogenous arc welding of stainless steel part 2: a kinetic model for nitrogen absorption and desorption. Weld J 2003;82:231S–7S.
[19] Suutala N, Takalo T, Moisio T. The relationship between solidification and microstructure in austenitic and austenitic-ferritic stainless steel welds. Metall Trans A 1979;10(4):512–4.
[20] Zhang X, Zhou Q, Wang K, Peng Y, Ding J, Kong J, et al. Study on microstructure and tensile properties of high nitrogen Cr-Mn steel processed by CMT wire and arc additive manufacturing. Mater Des 2019;166:107611.
[21] Elmer JW, Allen SM, Eagar TW. Microstructural development during solidification of stainless steel alloys. Metall Trans A 1989;20(10):2117–31.
[22] Jiang Z, Li H, Chen Z, Huang Z, Zou D, Liang L. The nitrogen solubility in molten stainless steel. Steel Res Int 2005;76:740–5.
[23] Li J, Li H, Liang Y, Liu P, Yang L. The microstructure and mechanical properties of multi-strand, composite welding-wire welded joints of high nitrogen austenitic stainless steel. Materials (Basel) 2019;12(18):2944.
[24] Hertzman S, Wessman S. An experimental and theoretical study of nitrogen flux in stainless steel TIG welds. Mater Sci Forum 1999;318–320:579–90.
[25] Shen YZ, Oh KH, Lee DN. Nitrogen strengthening of interstitial-free steel by nitriding in potassium nitrate salt bath. Mater Sci Eng A 2006;434(1–2):314–8.
[26] Li J, Huo J, Chen Y. Mechanism of improvement on strength and toughness of H13 die steel by nitrogen. Mater Sci Eng A 2015;640:16–23.

[27] Gavriljuk V, Berns H. High nitrogen steels: structure, properties, manufacture, applications. 1st ed. New York: Springer; 1999. p. 235–6.
[28] Schaeffler AL. Constitution diagram for stainless steel weld metal. Metal Prog 1949;56(11). 680-680B.
[29] Kotecki D, Siewert T. WRC-1992 constitution diagram for stainless steel weld metals: a modification of the WRC-1988 diagram. Weld Res Suppl 1992:171s–8s.
[30] Fan Z, Gao F, Wang Y, Men H, Zhou L. Effect of solutes on grain refinement. Prog Mater Sci 2021:100809.
[31] Gottstein G. Physical foundations of materials science. 1st ed. New York: Springer; 2004. p. 362–4. https://doi.org/10.1016/j.pmatsci.2021.100809. https://www.sciencedirect.com/science/article/pii/S0079642521000335.
[32] Gavriljuk V, Berns H. High nitrogen steels: structure, properties, manufacture, applications. 1st ed. New York: Springer; 1999. p. 2–4.
[33] Sabirov I, Murashkin MY, Valiev RZ. Nanostructured aluminium alloys produced by severe plastic deformation: new horizons in development. Mater Sci Eng A 2013;560(JAN.10):1–24.
[34] Ryen Ø, Holmedal B, Nijs O, Nes E, Sjölander E, Ekström H. Strengthening mechanisms in solid solution aluminum alloys. Metallurgical and Materials Transactions A 2006;37(6):1999–2006.